www.nature.com/scientificreports

scientific reports

Check for updates

OPEN

Mechanism of one-step hydrothermal nitric acid treatment for producing high adsorption capacity porous materials from coal gasification fine slag

Yunxuan Luoyang[1], Hua Wang[1,2]✉, Jian Li[1], Bi Chen[1], Xia Li[1] & Zhang Guotao[1]

The increasing amount of coal gasification fine slag (CGFS) necessitates its resource utilization. CGFS, mainly composed of porous carbonaceous particles and partially fused spherical or agglomerated ash particles, is an inexpensive and high-quality raw material for preparing adsorbent materials. However, the challenge remains in developing a simple, low-cost, and environmentally friendly method to produce high-performance porous materials from CGFS. In this study, a one-step treatment method using 2 mol/L nitric acid under hydrothermal conditions was proposed for CGFS. The adsorbent material (CGFS-2 M) prepared under a solid–liquid ratio of 2:5 and an initial concentration of 200 mg/L methylene blue (MB) exhibited an equilibrium adsorption capacity as high as 210.20 mg/g. The excellent adsorption performance of CGFS-2 M can be attributed to several factors: acid leaching for mineral removal and pore formation, resulting in a specific surface area and total pore volume 2.2 and 1.6 times that of untreated CGFS, respectively, and an optimized mesoporous pore size distribution favorable for MB adsorption; optimal mineral removal and a well-defined carbon microcrystal structure providing more space for MB adsorption; nitric acid treatment increasing the surface oxygen content and hydrophilicity, enhancing its ability to remove MB. The synergistic effect of pore structure improvement and surface modification indicates a feasible research direction for enhancing the performance of CGFS-based adsorbent materials. These results provide theoretical support for the development of efficient CGFS-based adsorbents.

Keywords Coal gasification fine slag, Hydrothermal nitric acid treatment, Porous materials, Adsorption

With the continuous advancement of coal gasification technology, the production of coal gasification fine slag (CGFS), a significant by-product, has been steadily increasing[1]. The urgent necessity of efficiently utilizing CGFS must be addressed promptly. CGFS primarily consists of aluminosilicates and residual carbon, with a high amorphous content, rendering it an ideal precursor for the preparation of porous adsorbent materials[2]. Nevertheless, CGFS exhibits complex and diverse physicochemical properties, and research on its utilization technologies remains relatively underdeveloped. At present, the methodologies for producing high-performance porous adsorbent materials from CGFS are not sufficiently mature[3]. To streamline the production process, reduce preparation costs, and overcome existing technological bottlenecks, it is imperative to undertake comprehensive and systematic research and optimization efforts.

Several reports have been published on the preparation of adsorbent materials from CGFS. For example, a highly efficient adsorbent for carbon dioxide capture was successfully prepared through flotation desilication followed by high-temperature alkali activation[4]. Another study used calcination desilication followed by chitosan composite for the removal of hexavalent chromium and RhB from water[5]. Additionally, a high-performance crystal violet adsorbent was prepared by first two-step acid desilication and then alkali activation[6]. MCM-41 mesoporous silica adsorbent was also prepared using alkali desilication solution[6]. However, these methods typically involve cumbersome experimental procedures and large amounts of chemical reagents, making the

[1]College of Chemistry and Chemical Engineering, Yulin University, Chongwen Road No.4, Yulin City 719000, Shaanxi Province, China. [2]Shaanxi Provincial Key Laboratory of Clean Utilization of Low-Modified Coal, Yulin University, Yulin City 719000, China. ✉email: 99452715@qq.com

preparation process complex and posing a high risk of environmental pollution, which is not conducive to industrial production. Although some scholars have also used simple acid leaching or alkali treatment to modify CGFS[7], they have focused solely on improving the pore structure without detailed discussions on the mechanism. Few studies have reported the synergistic enhancement of adsorption performance by simultaneously increasing pore structure and active sites. Therefore, there is an urgent need to explore a new method for preparing porous materials based on CGFS that considers factors such as process simplicity, low energy consumption, and environmental friendliness. This research aims to not only ensure excellent adsorption performance but also promote the high-value utilization of CGFS resources, which will be of great significance for theoretical innovation and technological progress in related fields.

The hydrothermal method is a commonly used approach for materials synthesis, promoting chemical reactions and crystal growth under high temperature and pressure conditions[8]. Nitric acid is a commonly used demineralization agent with strong oxidizing ability[9]. Due to the strong corrosiveness and oxidizing nature of nitric acid, this study proposes a strategy for the one-step hydrothermal acid leaching of coal gasification fine slag to prepare porous adsorbent materials, aiming to achieve simultaneous pore formation and surface modification of the materials. Moreover, this method does not employ the traditional atmospheric pressure treatment with nitric acid; instead, it uses a nitric acid treatment process in a hydrothermal closed environment. This choice enhances the dual effects of nitric acid treatment efficiently and promotes environmentally friendly experimental conditions.

Based on the unique structural composition of CGFS, this method fully utilizes the strong corrosiveness of nitric acid to effectively leach out some metal oxides in CGFS, thereby releasing the internal pore structure of residual carbon particles and etching the surface of some spherical ash particles to form a rich pore network. Furthermore, this method utilizes the strong oxidizing property of nitric acid to oxidize organic carbon and inorganic components in CGFS during the "pore formation" process, thereby altering the surface properties of the material and increasing active adsorption sites. Through the synergistic effect of structure and surface properties, a one-step method for preparing high-performance adsorbent materials is achieved. Compared with traditional processes, this method simplifies the process, reduces environmental risks and energy consumption, achieves synergistic optimization of pore structure and active sites, and has good industrial potential.

Materials and methods

Materials and reagents

Gasification slag samples were obtained from Qingshui Industrial Park, Yulin, Shaanxi. The gasification slag was dried and sieved through a 200-mesh sieve, and the resulting sample was labeled as CGFS. The chemical composition of the sample after high-temperature de-ashing of CGFS is shown in Table S1. Nitric acid and MB were procured as analytical reagent grade from Tianjin Kemi Chemical Reagent Co., Ltd. The experimental water was deionized water.

CGFS hydrothermal acid leaching test and adsorption experiment

The flow of the nitric acid hydrothermal acid leaching experiment is shown in Figure S1. The conditions of hydrothermal acid leaching with nitric acid were optimized using leaching rate as the test index. The optimized process parameters were acid concentration (1–10 mol/L), temperature (360–480 K), solid–liquid ratio (1:10–1:20) and time (60–150 min). The optimized experimental results are shown in Figure S2. Because the acid concentration has the greatest effect on the leaching rate, the subsequent discussion in this paper will focus on the effect of acid leaching concentration on the structure and composition of CGFS. The acid leach residue after acid leaching of CGFS with different concentrations of nitric acid was recorded as CGFS-X, where X represents the concentration of nitric acid used.

Precisely weigh specified amounts of CGFS-X samples (X = 1 M, 2 M, or 4 M) and introduce them into a solution with an initial MB concentration of 200 mg/L, maintaining a solid-to-liquid ratio of 2:5. Subject the mixture to agitation at room temperature. At designated intervals, withdraw samples for analysis and determine the MB concentration in the solution.

Sample analysis and structural characterization

The mineral phase composition of the samples was analyzed by X-ray diffraction (XRD, Bruker D8 Advance) using a Cu Kα radiation source with a scan range of 10° to 80° and a step size of 0.02°. Scanning electron microscopy (SEM, SIGMA 300) was employed to observe the surface morphology of the samples at various magnifications to capture detailed microstructural features. The composition of the surface functional groups was analyzed by Fourier-transform infrared spectroscopy (FTIR, Bruker Tensor 27) in the wavenumber range of 4000 cm^{-1} to 400 cm^{-1} with a resolution of 4 cm^{-1}. The surface composition of the samples was examined by X-ray photoelectron spectroscopy (XPS, Thermo Scientific K-Alpha) with an analysis chamber pressure below 2.0×10^{-7} mbar and using a non-monochromatic Al Kα X-ray source. The full-spectrum scanning flux energy was 150 eV, with a step of 1 eV; the narrow-spectrum scanning flux energy was 50 eV, with a step of 0.1 eV. Raman spectroscopy (Raman, Horiba LabRAM HR Evolution) was utilized to determine the microstructure of carbon with a laser excitation wavelength of 532 nm and a spectral resolution better than 1 cm^{-1}. Inductively coupled plasma optical emission spectroscopy (ICP-OES, Agilent 5110) was applied to analyze the elemental composition of CGFS and CGFS-X, with sample digestion carried out in a microwave-assisted system and using a standard addition method for quantification.The specific surface area, pore size, and volume of the samples were determined by a nitrogen adsorption and desorption analyzer (ASAP 260) at 77 K, sing the BET (Brunauer–Emmett–Teller) method for monolayer adsorption capacity and the BJH (Barrett-Joyner-Halenda) method for pore size distribution analysis. The absorbance of Methylene Blue (MB) was measured at 664 nm using a visible spectrophotometer

(Elite Technology Instrument Co., Ltd. 722N), with a calibration curve prepared over a concentration range of 0–10 mg/L to ensure accuracy.

Results and discussion

Impact of hydrothermal nitric acid treatment on the composition of CGFS

Impact on elemental composition

Table S2 presents the concentrations of more than 60 inorganic ash-forming elements detected in CGFS and CGFS-X. The analysis results indicate that, aside from Si, which shows an enrichment trend in CGFS-X, only a few elements, such as Ag in CGFS-2 M and CGFS-4 M , Bi in CGFS-2 M, and In and Se in the CGFS-1 M, exhibit enrichment. Conversely, all other elements display a significant leaching trend, suggesting that nitric acid hydrothermal leaching is effective the extraction of minerals.

To ensure data consistency in the classification of the 60 elements with concentrations above the detection limit, we standardized the raw data. Based on this standardized data, hierarchical clustering was performed. The results, depicted in the dendrogram in Fig. 1, categorize the data into two clusters, labeled A and B. Cluster A includes up to 45 elements, whose leaching rates do not improve significantly with increasing nitric acid concentration. In contrast, Cluster B comprises 15 elements, whose leaching rates show a marked increase with higher nitric acid concentrations.

Comparative analysis of the two clusters reveals differences in their response to changes in nitric acid concentration. This variability can be attributed to the distinct modes of occurrence of these elements in the original gasification slag[10]. Elements in Cluster A are more likely to be associated with aluminosilicate, carbonate, and sulfate minerals, whereas elements in Cluster B are probably present as iron oxides or phosphates[11]. This differentiation underscores the influence of the initial mineralogical composition on the leaching efficiency of nitric acid hydrothermal treatment.

The impact on the phase composition

The XRD patterns of CGFS and CGFS-X (X = 1 M, 2 M, 4 M, 10 M) are illustrated in Fig. 2. The primary inorganic minerals detected in CGFS include gehlenite ($Ca_2Al_2SiO_7$), quartz (SiO_2), hematite (Fe_2O_3), and magnetite (Fe_3O_4). With increasing nitric acid concentration, the characteristic diffraction peaks of $Ca_2Al_2SiO_7$ in CGFS-2 M, CGFS-4 M, and CGFS-10 M nearly disappear, while the characteristic diffraction peaks of SiO_2 increase. This indicates that higher concentrations of nitric acid lead to the precipitation of more free SiO_2 from $Ca_2Al_2SiO_7$[12], which is consistent with the increase in Si content with rising nitric acid concentration as shown in Table S2. Furthermore, the characteristic diffraction peaks of Fe_3O_4 also diminish with increasing nitric acid concentration. This is due to Fe_3O_4, being a basic oxide, undergoing redox reactions with the strong oxidizing acid nitric acid. After the dissolution of Fe_3O_4 by nitric acid, the remaining nitric acid oxidizes Fe^{2+} in the acid leachate to Fe^{3+}[13]. The characteristic diffraction peaks of Fe_2O_3 and SiO_2 do not show significant enhancement with increasing nitric acid concentration, indicating that concentrations above 2.0 mol/L do not markedly improve the leaching efficiency of Fe_2O_3 and SiO_2.

As the concentration of nitric acid increases, CGFS-X exhibits distinct "bread-like" peak structures in the diffraction angle range of $2\theta = 20–30°$, suggesting the presence of substantial amorphous substances in these acid leaching residues[14]. The evolution of amorphous substances in CGFS-X is associated with the partial degradation of inorganic minerals (such as $Ca_2Al_2SiO_7$ and Fe_3O_4) and the formation of poorly crystalline or non-crystalline materials[15]. In addition to containing amorphous aluminosilicates and SiO_2, CGFS also includes a significant amount of amorphous carbon.

Impact of hydrothermal nitric acid treatment on the microstructure of CGFS

Impact on the microscopic surface morphology

As shown in Fig. 3, SEM images of the CGFS and CGFS-X samples illustrate their microstructural characteristics. In Fig. 3a, the untreated CGFS is observed to comprise several components: partially clogged porous char particles (A), smooth-surfaced fully molten inorganic components (B), and rough-surfaced partially molten agglomerated inorganic components (C). After nitric acid demineralization treatment, the smooth spherical inorganic components in the CGFS-X (X = 1 M, 2 M, 4 M) samples are almost entirely absent (Fig. 3b–d). This disappearance can be attributed to two major factors: first, some of these spheres consist of metal oxides (such as Ca, Mg, Na) that are readily dissolved by nitric acid[16]; second, the leaching of soluble metal elements from these spheres renders their surfaces rough and porous (as seen in D), rather than smooth. The partially molten agglomerates, enriched with acid-insoluble elements (such as Si and Al), remain even after treatment with nitric acid.

Compared to CGFS, the CGFS-X samples obtained after nitric acid treatment exhibit a more open pore structure. As the acid concentration increases, the extent of surface agglomeration decreases, leading to a more developed porous structure with a noticeable reduction in pore size. Figure 3c shows that the surface of the residue treated with 2.0 mol/L nitric acid is the smoothest, with the least residual agglomerated inorganic components. However, when the concentration of nitric acid is increased to 4.0 mol/L, the severe corrosiveness of the acid significantly erodes the char framework, resulting in denser pore channels, thinner carbon layers, and a rougher surface.

Influence on the microstructure of carbon crystals

Raman spectroscopy is extensively employed for the structural characterization and defect analysis of carbonaceous materials[17]. Figure S3 displays the Raman spectra of CGFS and CGFS-X (X = 1 M, 2 M, 4 M) samples. Prominent D and G peaks are observed in the first-order region (1100–1800 cm^{-1}), along with comparatively weaker vibrational peaks of C–H and other groups in the second-order region (2200–3400 cm^{-1})[18]. A higher

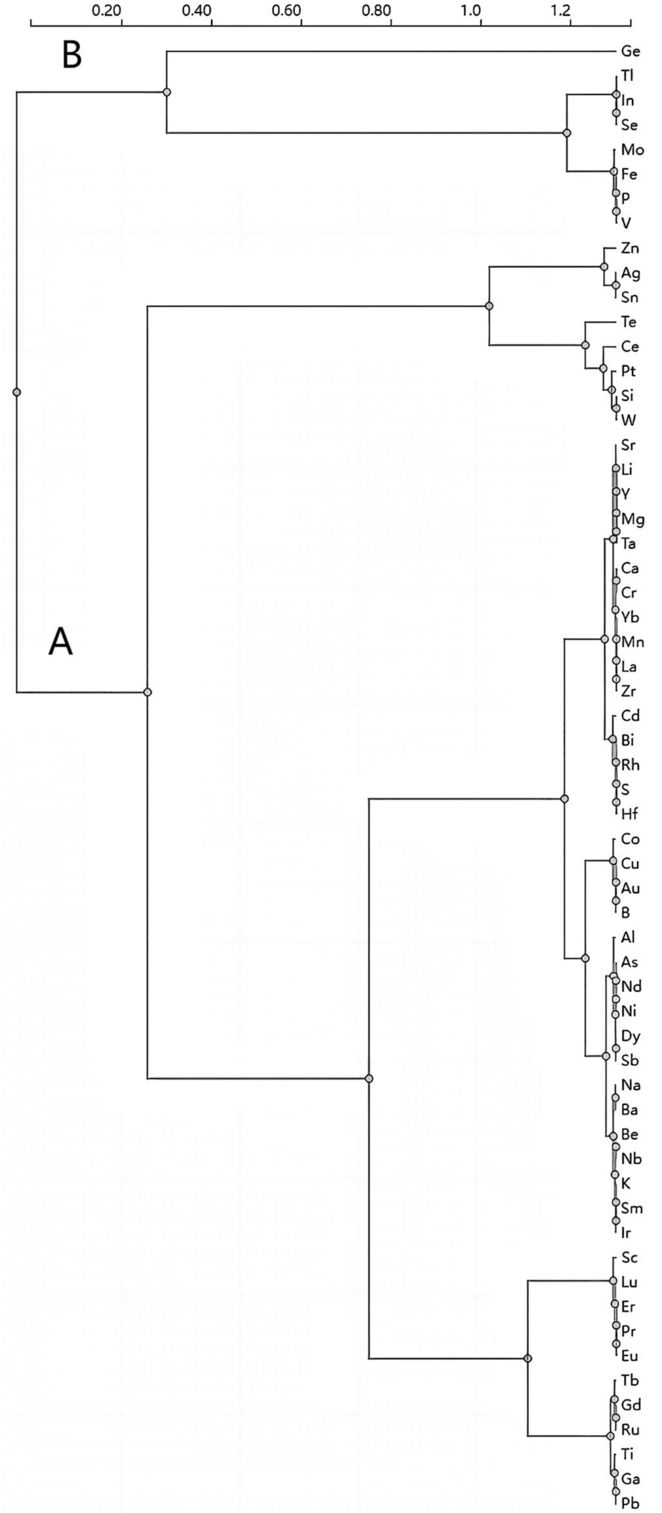

Fig. 1. Clustering dendrogram of elements.

D band, located between 1327 and 1350 cm^{-1}, indicates a greater content of amorphous carbon in the residual material, whereas the G band, observed at 1579–1598 cm^{-1}, is attributed to the stretching vibrations of aromatic layers in the graphite structure[19]. This implies that a stronger G band signifies a higher degree of graphitization.

It is highlighted that the overlap between the D and G bands can lead to the loss or neglect of characteristic information pertaining to highly disordered carbonaceous materials when relying solely on the D and G band Raman spectra[20]. Therefore, further deconvolution (peak fitting) of the Raman spectra of coal is necessary to extract hidden information about the skeletal carbon structures in the overlapping region. To achieve precise

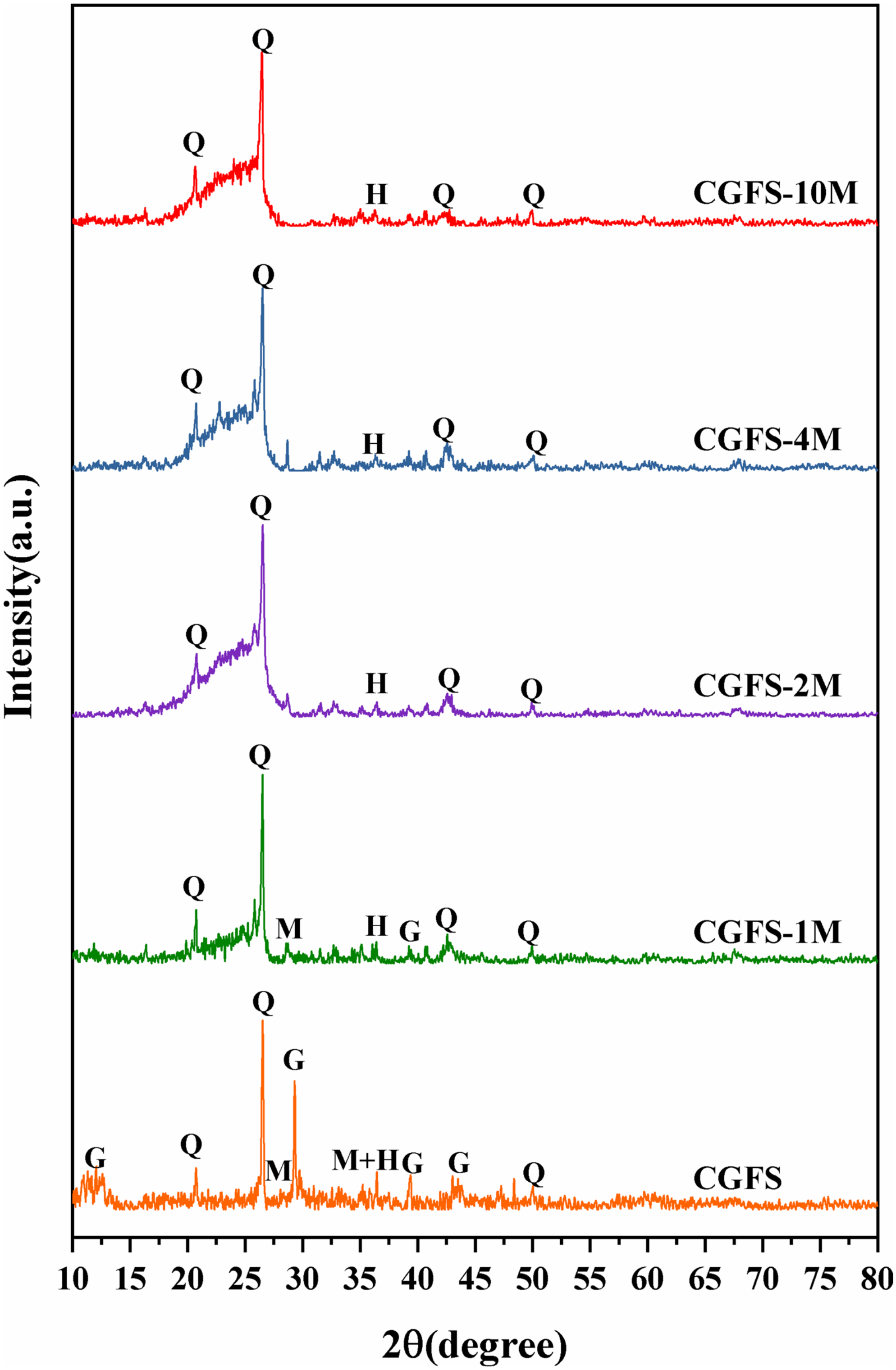

Fig. 2. XRD patterns of CGFS and CGFS-X. (Mineral abbreviations: Q = quartz, G = gehlenite, H = hematite, M = magnetite.)

spectral parameters, particularly the integral intensity ratio, the Raman spectra were deconvoluted into five peaks (D_1, D_2, D_3, D_4, G) according to the method proposed by Sadezky et al.[21], as depicted in Fig. 4.

The D_1 band typically represents defect structures and is associated with the planar vibrations of sp^2 carbon atoms with structural defects, edge carbon atoms, and impurity atoms[22]. The D_2 band appears as a shoulder of the G band and corresponds to the E 2 g vibrational mode at the surface of graphite layers[23]. The G peak arises from the vibrations of the ideal graphite lattice. The D_3 peak corresponds to sp^2-bonded amorphous carbon, including

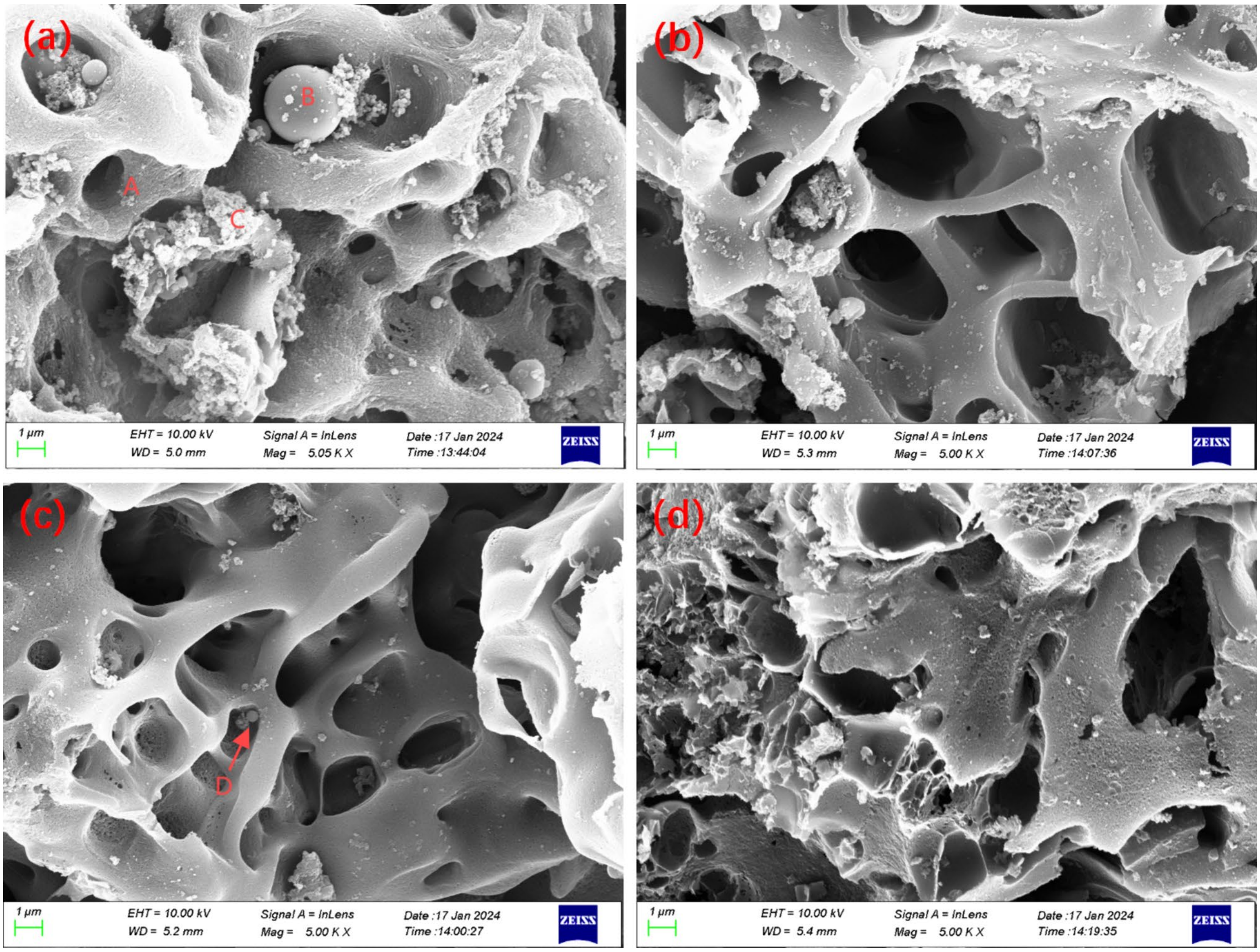

Fig. 3. SEM images of (**a**) CGFS, (**b**) CGFS-1 M, (**c**) CGFS-2 M, and (**d**) CGFS-4 M.

organic molecules and functional groups[23]. The D_4 peak's formation is attributed to sp^2-sp^3 hybrid bonds or C–C and C=C stretching vibrations at the periphery of microcrystallites, forming structures similar to polyolefins [24].

Using the peak intensity ratio I_D/I_G as an indicator for evaluating the structural order of carbon in the samples, an increase in the I_D/I_G ratio suggests a higher degree of disorder in the carbon microcrystalline structure and a lower degree of graphitization[19]. As shown in Table 1, the I_D/I_G ratios for CGFS-X are all lower than that for CGFS, indicating that the degree of graphitization of CGFS has improved following hydrothermal nitric acidacid leaching. The I_D/I_G ratio of CGFS-2 M is lower than those for CGFS-1 M and CGFS-4 M, suggesting that CGFS-2 M has the highest degree of graphitization. When the concentration of nitric acid increases from 2.0 to 4.0 mol/L, the I_D/I_G value increases. This is because, during the acid leaching process, the increasing concentration of nitric acid can etch the carbon structure and expand the spacing within the carbon network, leading to a decrease in the degree of graphitization for CGFS-4 M.

A_{D3+D4}/A_{All} can be used to indicate the active site of carbon, the higher the ratio, the more active site[19]. A_{D1}/A_G is related to the degree of disorder in the carbon microcrystalline structure[25], A_{D4}/A_{All} can be described as the relative number of cross-linking bonds, and $A_{D3}/A_{G+D2+D3}$ is used to characterize the degree of amorphousness in the carbon microcrystalline structure[19]. CGFS-4 M showed an increase in A_{D1}/A_G and $A_{D1+D2+D3+D4}/A_G$ compared to CGFS, implying that acid leaching with 4.0 mol/L of nitric acid could change the microstructure of CGFS. In contrast, CGFS-2 M exhibited lower A_{D1}/A_G values, indicating that the carbon microcrystalline structure of CGFS acid-impregnated with nitric acid concentration of 2.0 mol/L had a low degree of disorder. CGFS-X showed a decrease in all $A_{D3}/A_{G+D2+D3}$ ratios as compared to CGFS, with the smallest ratio of 0.2370 for CGFS-2 M This indicates that nitric acid has a significant effect on the amorphous carbon structure of CGFS, with 2.0 mol/L of nitric acid having a more pronounced effect on the degree of crystallinity of the carbon microcrystalline structure. Additionally, since nitric acid treatment of CGFS resulted in a significant increase in A_{D3+D4}/A_{All}, it illustrated that nitric acid also had a significant impact on the active sites of carbon.

Effect of hydrothermal nitric acid treatment on pore structure

N_2 adsorption/desorption isotherm analysis

As shown in Fig. 5a, N_2 adsorption/desorption isotherms of CGFS and acid-impregnated slag CGFS-X are similar to the type IV isotherms. In the lower relative pressure (P/P_0) interval, the adsorption/desorption isotherm

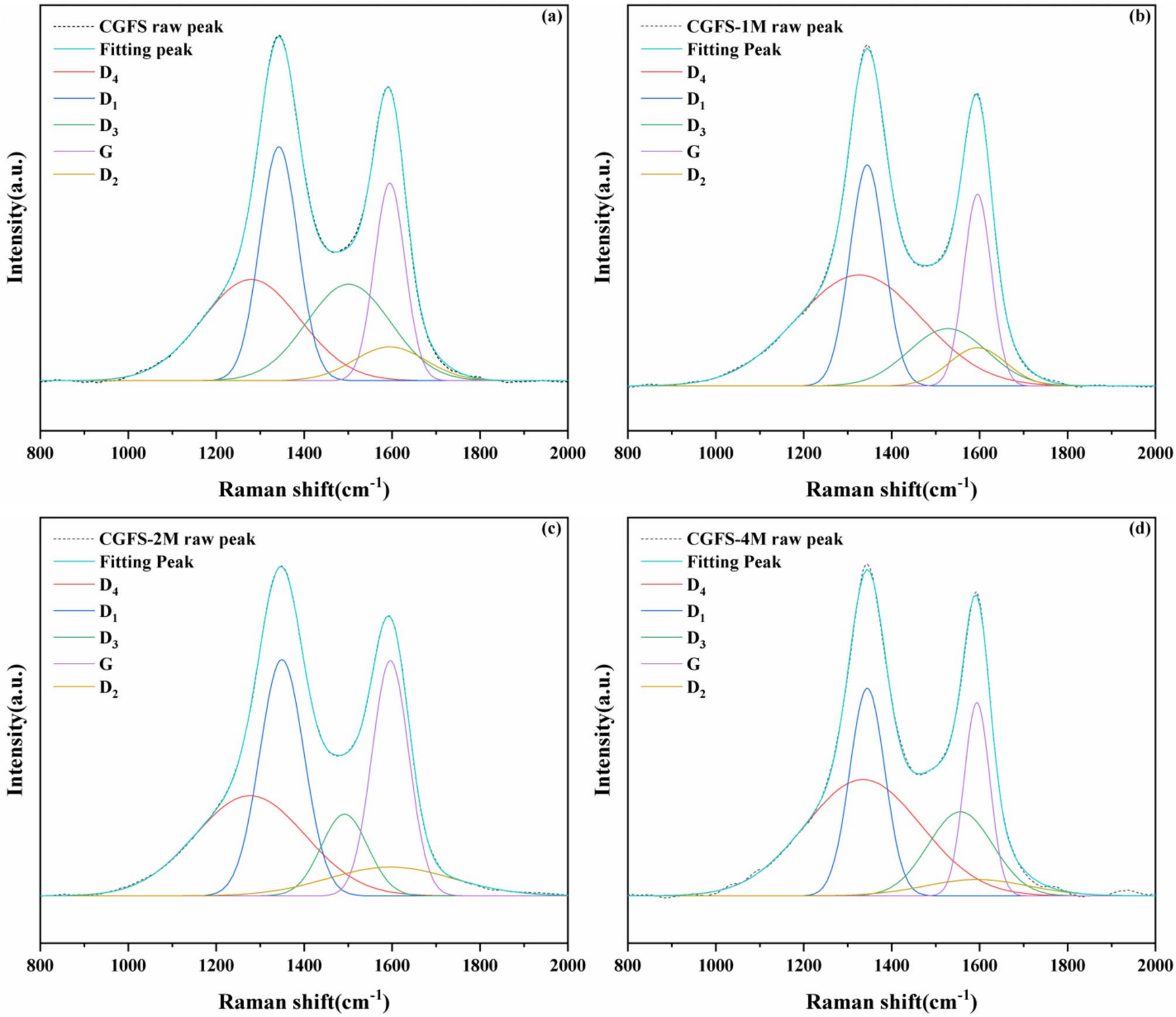

Fig. 4. Raman spectra of the CGFS and CGFS-X.

Samples	I_D/I_G	A_{D3}/A_{All}	A_{D4}/A_{All}	A_{D3+D4}/A_{All}	$A_{D3}/A_{G+D2+D3}$	$A_{D1+D2+D3+D4}/A_G$	A_{D1}/A_G
CGFS	1.1837	0.2293	0.2800	0.0002	0.4889	4.8449	1.4662
CGFS-1 M	1.1533	0.1340	0.4147	0.5486	0.3754	5.3340	1.4480
CGFS-2 M	1.0044	0.1014	0.2934	0.3954	0.2370	3.3340	1.2044
CGFS-4 M	1.0745	0.1658	0.4108	0.5767	0.4502	5.6363	1.4649

Table 1. Carbon microstructure parameters of samples.

curves of CGFS-X basically overlap and show a significant upward bulge, a phenomenon that implies that the surface of CGFS-X is dominated by monolayer adsorption. The turning point at this bulge marks the saturation point of monolayer adsorption, which in turn indicates the presence of microporous structure, in agreement with the discussion in the literature[26]. With the increase of P/P_0 to approximately 0.4, the phenomenon of hysteresis loops appears, which marks the transition from monolayer adsorption to multilayer adsorption, as well as the accompanying generation of a large number of mesopores.

In the high P/P_0 region, CGFS-X undergoes capillary coalescence, which is manifested by a sharp rise in isotherms. The presence of a small amount of macroporous formation can be inferred at conditions close to the unit relative pressure[27]. It is noteworthy that the isotherms of the desorption process do not replicate the trajectory of the adsorption process, which is mainly due to the adsorption hysteresis phenomenon caused by capillary coalescence[28]. This deviation reflects the irreversible character of the adsorption and desorption processes and implies a significant influence exerted by the microstructure of the material on its adsorption properties.

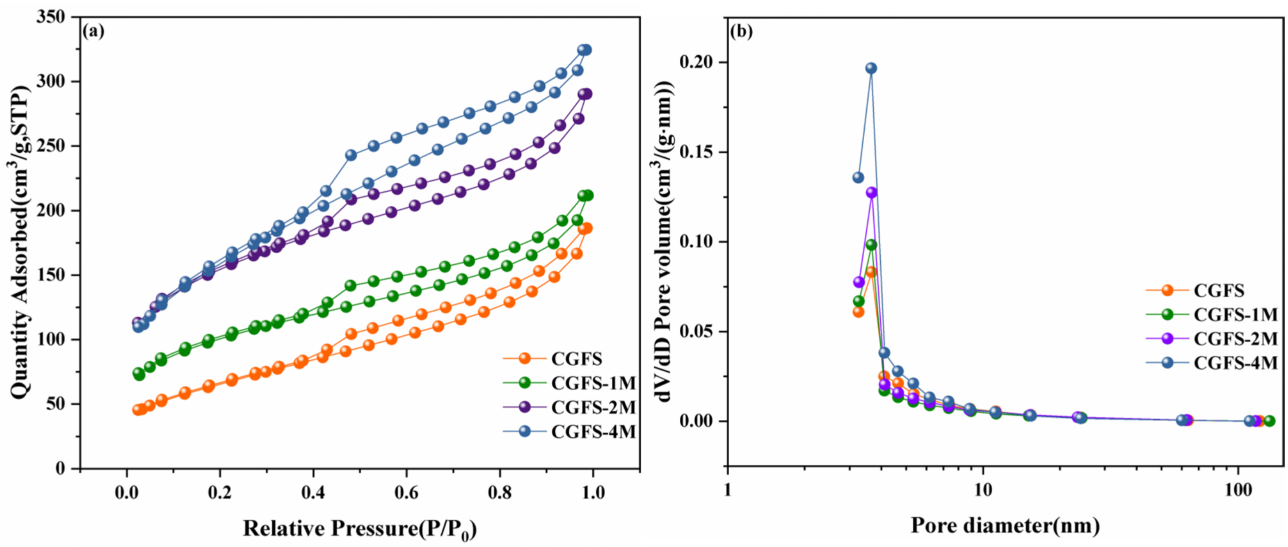

Fig. 5. (**a**) N_2 adsorption/desorption isotherms and (**b**) pore size distribution of CGFS and CGFS-X.

In N_2 adsorption/desorption isotherm analyses of the four samples, it was observed that the nitrogen adsorption at consistent relative pressure points showed a clear sequential ordering, from high to low, of CGFS-4 M, CGFS-2 M, CGFS-1 M, and CGFS.This ordering revealed a trend: as the concentration of the nitric acid treatments increased, the pore structure of the samples became progressively more developed, and accordingly, the specific surface area also increased significantly. This phenomenon characterizes the significant influence of nitric acid concentration on the pore characteristics and specific surface area of the materials, suggesting that nitric acid treatment plays a key role in optimizing the pore structure and enhancing the adsorption performance of the materials.

Pore size distribution analysis

Figure 5b demonstrates the pore size distribution diagrams of the four materials, revealing that all of these materials exhibit a hierarchical porous structure of macropores, mesopores and micropores, with a high distribution density especially at the mesopore level. According to the statistical results of the porous structure parameters of the materials in Table 2, the specific surface area and total pore volume of the acid-impregnated residue showed an increasing trend with the increase of nitric acid concentration, while the mean pore diameter showed a decreasing trend. Specifically, the specific surface area and total pore volume of the 4 mol/L acid-impregnated residue were 2.39 and 1.74 times that of the original gasified fine residue, respectively; while its mean pore diameter was 0.73 times that of the original gasified fine residue.

It is crucial to note that as the concentration of nitric acid increases, the specific surface area and total pore volume of CGFS-X exhibit an increasing trend. For example, when the nitric acid concentration was raised from 1 to 2 mol/L, these parameters increased by 175.18 m^2/g and 0.122 cm^3/g, respectively. However, with a further increase in concentration from 2 to 4 mol/L, the increments in specific surface area and total pore volume were only 44.01 m^2/g and 0.053 cm^3/g, respectively. Additionally, when the nitric acid concentration increased from 1 to 2 mol/L, the pore diameter decreased by 0.36 nm. In contrast, when the concentration increased from 2 to 4 mol/L, the pore diameter did not decrease but instead increased by 0.1 nm. This observation suggests that excessive nitric acid concentrations may compromise the carbon structural skeleton during the process of intense pore etching, corroborating the results of SEM analysis.

Pore fractionation characterization

Using low-temperature nitrogen adsorption data, the fractal Frenkel-Halsey-Hill (FHH) model was used to calculate the fractal dimension values (D) that could reflect the degree of pore development of the four materials[29]. The fractal dimension values were calculated as Eqs. (1) and (2)[30]:

Sample	Specific surface area (m^2/g)	Aperture diameter (nm)	Total pore volume (cm^3/g)
CGFS	234.82	4.92	0.289
CGFS-1 M	342.21	3.84	0.328
CGFS-2 M	517.39	3.48	0.450
CGFS-4 M	561.40	3.58	0.503

Table 2. Specific surface area and pore distribution of CGFS and CGFS-X.

$$\ln(V) = b + A\ln\left(\ln\left(\frac{p_0}{p}\right)\right) \quad (1)$$

$$D = A + 3 \quad (2)$$

where V is the volume of N_2 adsorbed at the equilibrium pressure P, and P_0 represents the saturation pressure of N_2. A is the power-law exponent dependent on the fractal dimension (D), and b is a constant. D takes values between 2 and 3.

N_2 adsorption/desorption curves at low ($P/P_0 < 0.4$) and high ($P/P_0 > 0.4$) pressures showed significant differences, and their fractal dimensions had different physical interpretations in different pressure intervals. Therefore, a critical point was set at $P/P_0 = 0.4$, and the curves were linearly fitted by the least squares method, respectively, and the fitting results are shown in Fig. 6. In the low-pressure interval, the calculated fractal dimension reflects the roughness of the microporous surface or the complexity of the microporous structure; while in the high-pressure interval, the fractal dimension reflects the roughness and complexity of the mesoporous and macroporous pore surfaces[30]. The low and high pressure fractal dimension values (denoted as D_1 and D_2, respectively) were calculated according to the fitted equations, and the results are shown in Table 3.

From the analysis presented in Table 3, it is evident that the fitted correlation values for various materials across different pressure stages are all greater than 0.9000, indicating a strong fit. Nitric acid treatment significantly enhances the D_1 value and exhibits an increasing trend with higher acid leaching concentrations, suggesting that nitric acid treatment facilitates the development of micropores in CGFS. This treatment also increases the roughness and structural complexity of the microporous surface, with the improvement effect intensifying with higher nitric acid concentrations. Regarding the D_2 value, nitric acid treatment similarly enhances the development of mesopores and macropores, although this improvement diminishes with excessive increases in

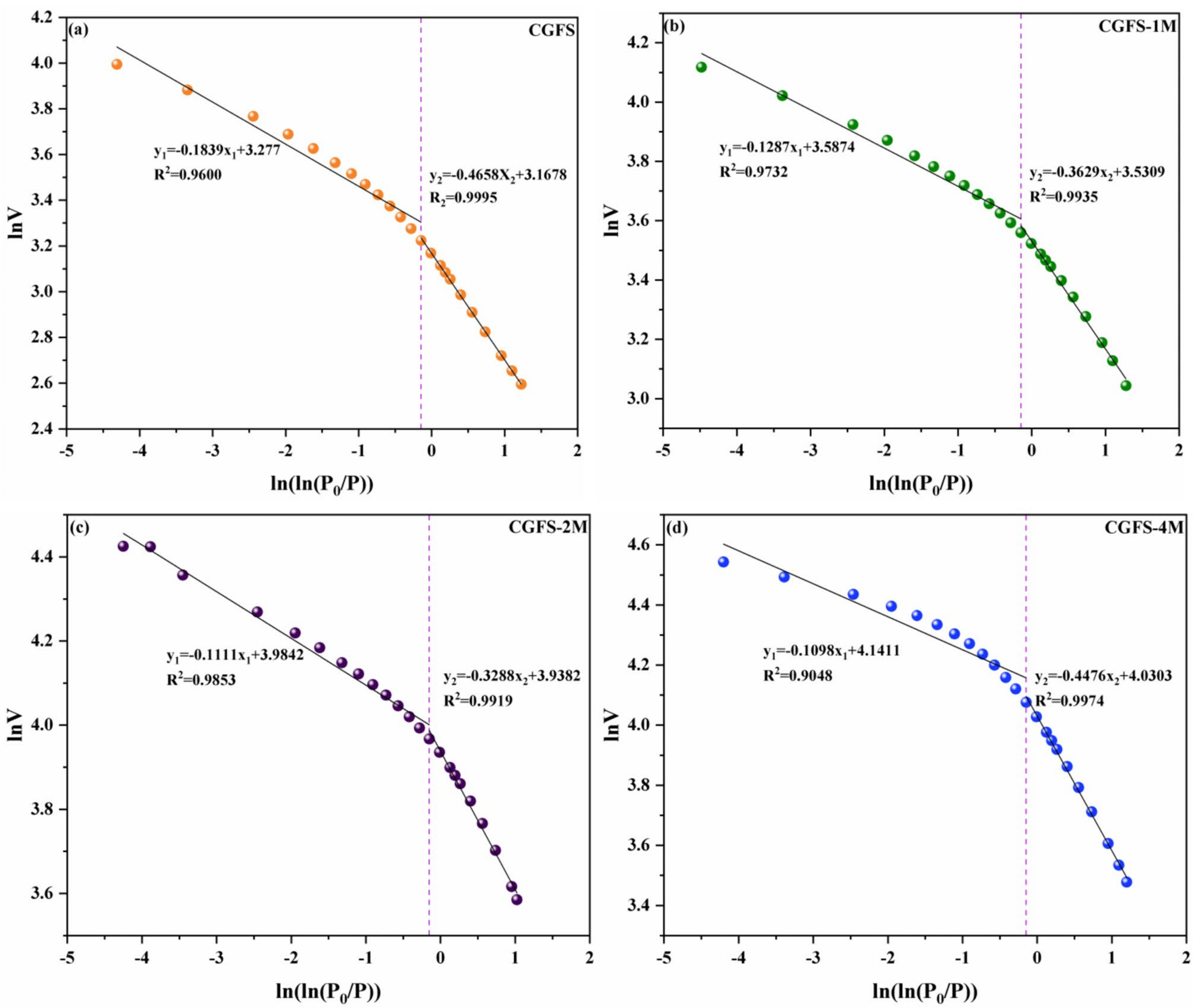

Fig. 6. Representative plots of CGFS and CGFS-X of lnV versus ln (ln (P_0/P)) on the basis of the N_2 adsorption isotherms.

Sample	$P/P_0 = 0\sim0.4$			$P/P_0 = 0.4\sim1.0$		
	A_1	D_1	R_1^2	A_2	D_2	R_2^2
CGFS	−0.1839	2.8161	0.96	−0.4658	2.5342	0.9995
CGFS-1	−0.1287	2.8713	0.9732	−0.3629	2.6371	0.9935
CGFS-2	−0.1111	2.8889	0.9853	−0.3288	2.6712	0.9919
CGFS-4	−0.1098	2.8902	0.9048	−0.4476	2.5524	0.9974

Table 3. Fractal dimensions of FHH model for CGFS and CGFS-X.

nitric acid concentration. For instance, when the nitric acid concentration was elevated from 2 to 4 mol/L, the D_2 value markedly decreased. This indicates that a moderate nitric acid concentration is beneficial for enhancing the development of mesopores and macropores, thereby improving their surface roughness and structural complexity. The findings on the impact of nitric acid treatment on the pore structure of gasification slag align with the previous analysis in Section "Impact on the microscopic surface morphology". Specifically, while higher concentrations of nitric acid treatment promote micropore etching, excessive treatment may compromise the stability of the carbon skeleton structure, adversely affecting the mesoporous and macroporous structures.

Effect of hydrothermal nitric acid treatment on the surface composition of CGFS

Effect on the composition of surface functional groups

The FTIR profiles of CGFS and CGFS-X are shown in Fig. 7a. The peak positions were attributed as follows: 3444 cm^{-1} corresponds to the stretching vibration of $-OH$[31]; 1612 cm^{-1} corresponds to the stretching vibration of C=C[32]; the peak at 1380 cm^{-1} is the stretching vibration of $-CH_3$ [33]; the range from 1073 cm^{-1} to 1050 cm^{-1} is the stretching vibration of Si–O–Al or Si–O–Si [34]; 789 cm^{-1} corresponds to the symmetric stretching vibration of Si–O[35]; and 464 cm^{-1} corresponds to the symmetric stretching vibration of Si–O–Si[36]. By comparing CGFS and the sample CGFS-X after nitric acid treatment, it can be found that nitric acid treatment (especially under

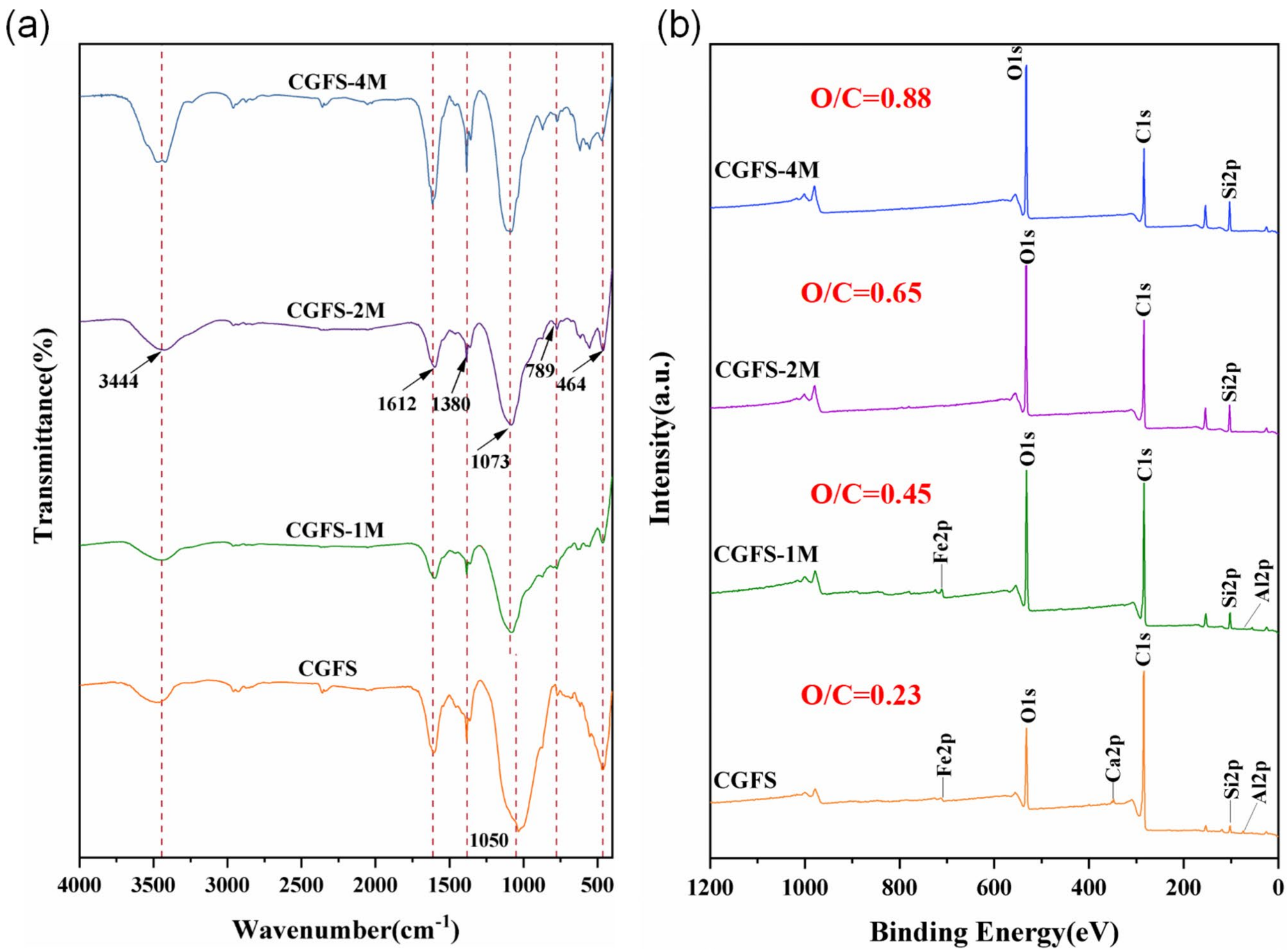

Fig. 7. (**a**) FTIR spectra and (**b**) XPS survey scan spectra of the CGFS and CGFS-X.

2 M and 4 M treatment conditions) significantly enhanced the vibrational strengths of functional groups such as –OH, Si–O–Al, and Si–O–Si in the sample. This indicates that the nitric acid treatment can effectively promote the formation or exposure of these functional groups.

Influence on surface elemental binding states
Figure 7b presents the full-spectrum scans of CGFS and CGFS-X, while Table 4 lists the atomic percentages of the major elements on the surface of each sample. With increasing concentrations of hydrothermal nitric acid treatment, the O/C ratio significantly increases, indicating that the strong oxidative properties of nitric acid facilitate the incorporation of oxygen-containing functional groups into CGFS. The atomic percentage of Si also shows a substantial increase with higher nitric acid treatment concentrations, which is consistent with the analysis in Section "Impact on elemental composition". This suggests that hydrothermal nitric acid treatment is ineffective at leaching silicate-based inorganic materials. In contrast, elements such as Fe, Al, and Ca are more readily leached by nitric acid, with even a 1 mol/L nitric acid treatment showing a notable leaching effect.

Figure 8a shows the deconvolution fitting results of the C 1 s high-resolution spectra for CGFS-X and CGFS. The peak positions correspond to non-oxidized carbon (C–C/C=C/C–H: 284.8 eV)[37], oxygenated carbon (C–O: 285.4 eV)[38], and carboxyl carbon (O–C=O: 289.2 eV)[39]. Among these, C–C/C=C/C–H is typically considered to be hydrophobic hydrocarbon chain functional groups[40]. Compared to CGFS, the content of C–C/C=C/C–H in CGFS-X is reduced, with CGFS-2 M exhibiting the lowest content at just 24.00%. This indicates that the hydrophobicity of CGFS decreases following nitric acid treatment, with the most significant reduction observed in CGFS-2 M.

The fitting results of the O 1 s spectra of the sample in Fig. 8b revealed the presence of the following chemical bonds: inorganic oxygen (such as Fe–O, i.e., at 530.3 eV)[41], carbonyl (C=O, at 531.4 eV)[42], hydroxyl (C–OH, at 532.5 eV)[43], and ether (C–O–C, at 533.5 eV)[44]. Compared to the original CGFS, the inorganic oxygen content of CGFS-1 M increased by 0.73%, indicating that the nitric acid treatment can dissolve the iron oxides encapsulated in the carbon. As shown in Table 5, compared to CGFS, the CGFS-X series samples exhibited increases in the contents of C=O, C–OH, and C–O–C. Among them, the increase in C–OH was the most significant, with increases of 7.01%, 15.35%, and 20.92%, respectively, suggesting that the nitric acid treatment can significantly increase the content of acidic functional groups on the CGFS surface, thereby enhancing the hydrophilicity of the material and its affinity for polar organic compounds.

The fitting results of the Fe 2p spectra shown in Fig. 8c indicate that the iron element exists in both divalent and trivalent chemical states[45]. Compared to the original GGFS sample, the relative content of trivalent iron in the GGFS-1 sample increased, which may be attributed to the strong oxidizing effect of nitric acid. In the CGFS sample treated with 2 mol/L nitric acid, the Fe 2p peak was barely observed, reflecting the excellent dissolution ability of nitric acid towards iron oxides.

The fitting results of the Si 2p XPS spectra in Fig. 8d show peaks at 102.7 and 103.5 eV, corresponding to aluminosilicates and silicon dioxide (SiO_2)[46], respectively. With the increase in nitric acid concentration, the SiO_2 content on the CGFS surface gradually increased, and the CGFS-4 M sample exhibited the highest SiO_2 content of 13.38%. Furthermore, the aluminosilicate content on the CGFS-X sample surface first increased and then decreased, with the CGFS-2 M sample having the maximum aluminosilicate content of 9.19%. This suggests that when the nitric acid concentration is increased to 2.0 mol/L, it effectively extracts aluminosilicates from the pores and carbon-encapsulated regions. At a concentration of 4.0 mol/L, the nitric acid treatment further leaches these species, enhancing the purification of the material.

Influence of nitric acid concentration on the adsorption performance of MB

As illustrated in Figure S4, CGFS-X significantly enhances the removal efficiency for MB, achieving a removal rate that is 2.7 to 2.9 times greater than that of untreated CGFS. To further investigate the effect of hydrothermal nitric acid treatment concentration on the adsorption performance of CGFS, the adsorption capacity (q_t) and removal rate (R) of MB by CGFS-X were compared under the same experimental conditions, as illustrated in Fig. 9. It is evident that, after 30 min of adsorption, CGFS-2 M exhibits the highest removal performance for MB, whereas the differences between CGFS-1 M and CGFS-4 M after 60 min of adsorption are not significant. In the first 30 min of adsorption, the trend line for the removal rate of MB by CGFS-4 M shows the steepest slope, indicating the fastest adsorption rate, which is attributed to its largest specific surface area. The slope of the removal rate trend line for CGFS-2 M is the second highest, while CGFS-1 M demonstrates the steepest slope within the first 20 min, but this slope decreases significantly between 20 and 30 min. After 30 min of adsorption, the adsorption rate of the CGFS-2 M sample significantly slowed down. At an adsorption duration of 150 min, CGFS-2 M demonstrated exceptional adsorption capacity and removal efficiency, achieving maximum values of

Samples	Element mass fraction (%)					
	C 1 s	O 1 s	Fe 2p	Si 2p	Ca 2p	Al 2p
CGFS	63.87	14.93	0.08	2.79	0.17	1.89
CGFS-1 M	52.51	23.79	0.50	6.17	0.08	0.38
CGFS-2 M	43.91	28.54	0.06	10.66	0.03	0.38
CGFS-4 M	38.18	33.69	0.04	13.77	0.02	–

Table 4. The atomic percentage of the main elements on the surface of CGFS and CGFS-X.

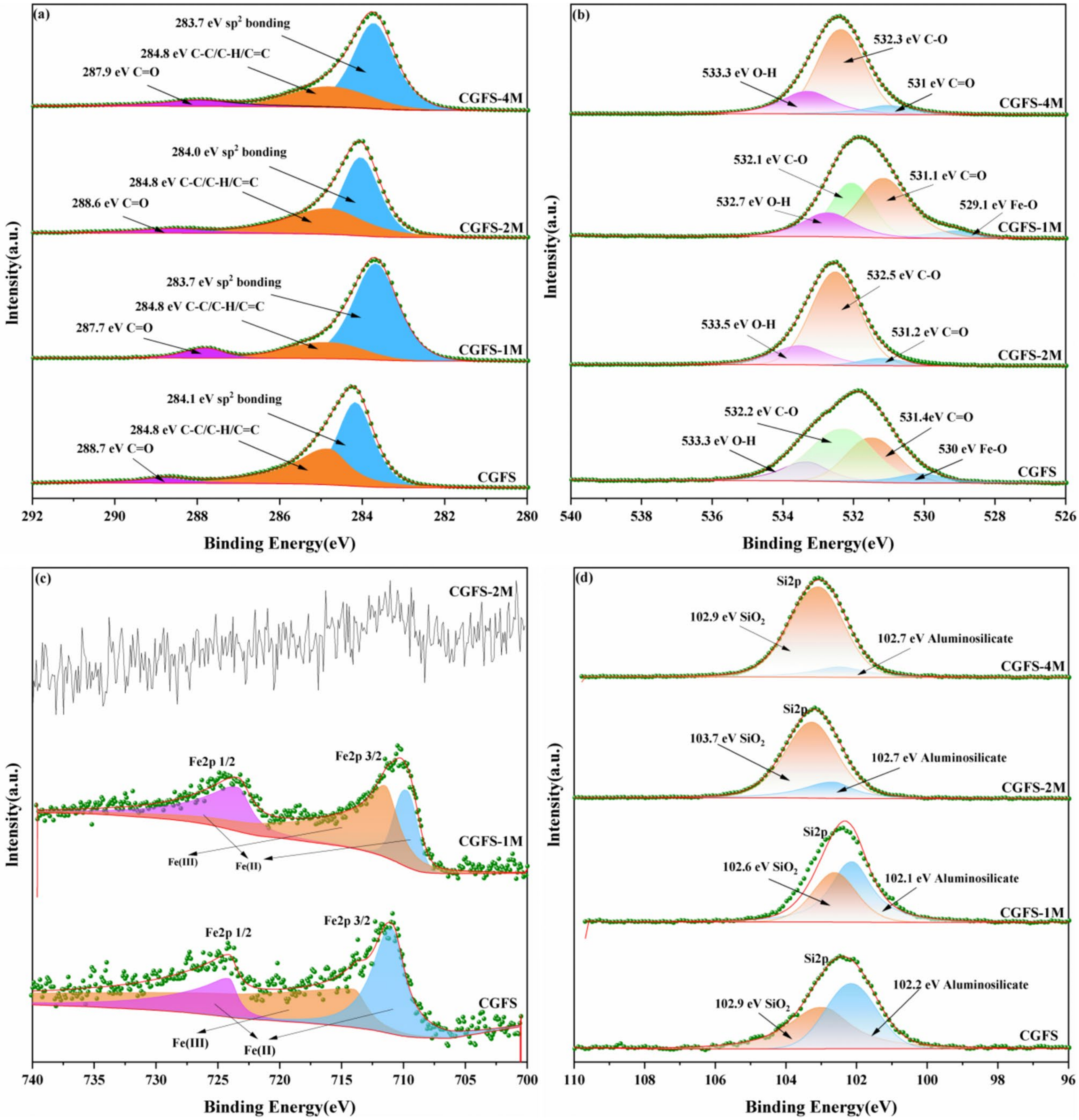

Fig. 8. XPS spectra of (**a**) C1s, (**b**) O1s, (**c**) Fe2p, and (**d**) Si2p in CGFS and CGFS-X.

Samples	Functional groups content (%)						
	C–C/C=C/C–H	C–O	O–C=O	C=O	C–OH	C–O–C	Fe–O
CGFS	42.92	29.47	5.21	5.65	6.25	5.27	0.96
CGFS-1 M	33.00	24.57	4.56	5.03	12.06	10.18	1.53
CGFS-2 M	24.00	25.19	3.52	9.36	18.85	6.34	——
CGFS-4 M	28.19	11.74	4.90	6.88	22.87	9.60	——

Table 5. Functional group content of CGFS and CGFS-X.

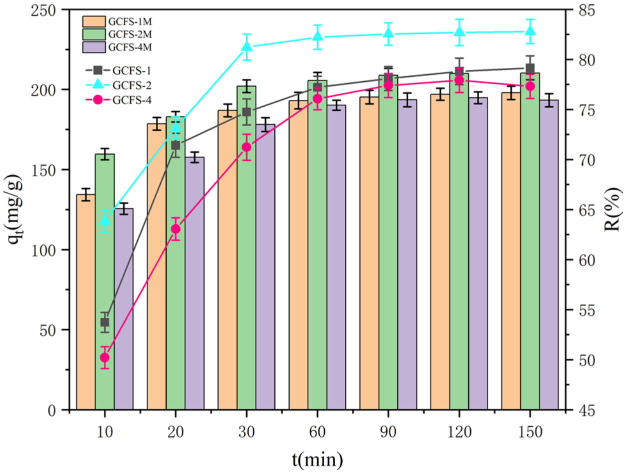

Fig. 9. Adsorption of Methylene Blue by CGFS-X (X = 1 M, 2 M, 4 M).

210.20 mg/g and 82.78%, respectively, which are significantly superior to those of the CGFS-1 M and CGFS-4 M samples. Additionally, the adsorption capacity of CGFS-2 M also outperformed various adsorbents derived from industrial waste reported in the literature (Table 6).

Exploration of the mechanism of hydrothermal nitric acid treatment of CGFS

Surface and composition modification by nitric acid treatment

Under hydrothermal conditions, nitric acid undergoes a series of chemical reactions with the carbon materials and minerals in CGFS. Nitric acid acts as a strong oxidizing agent and undergoes oxidation reactions with the carbon in the carbon materials to produce oxygen-containing functional groups such as carboxyl, hydroxyl and nitro groups (as described in 3.4). These functional groups increase the polarity and chemical activity of the carbon surface, enabling it to form hydrogen bonds or electrostatic interactions with the pollutant molecules[53], thus improving the adsorption efficiency. The specific chemical reaction equations are as follows.

$$C + 2HNO_3 \rightarrow CO_2 + 2NO_2 + H_2O \tag{1}$$

$$R + HNO_3 \rightarrow R - OH + NO_2 + H_2O \tag{2}$$

$$R + 2HNO_3 \rightarrow R - COOH + 2NO_2 + H_2O \tag{3}$$

$$R + HNO_3 \rightarrow RC = O + NO_2 + H_2O \tag{4}$$

Nitric acid undergoes acid–base neutralization reaction with alkaline components (e.g., oxides, carbonates) in CGFS to produce corresponding nitrates and water.

$$MO_{x/2} + xHNO_3 \rightarrow M(NO_3)x + \frac{x}{2}H_2O \tag{5}$$

where M represents a metal ion.

$$\text{CaCO3} + 2HNO_3 \rightarrow \text{Ca}(NO_3)_2 + CO_2 + H_2O \tag{6}$$

Precursor for adsorbent	The highest adsorption capacity (mg/g)	References
Steel converter slag	41.62	47
Composite foams containing alkali-activated blast furnace slag and lignin	39.5	48
Blast furnace slag	60.35	49
Fly ash	28.65	50
Coal gasification slag	19.18	51
Coal gasification fine slag	140.57	52
Coal gasification fine slag	210.20	This study

Table 6. Reported MB adsorption capacities of adsorbents prepared from wastes in the literature.

Silicates and nitric acid can also undergo a variety of chemical reactions in hydrothermal environments, such as the acidolytic reaction of nitric acid on silicates[54], the generation of different forms of silicon oxides, and the gelation reaction of silicates. The possible reaction equations are as follows:

$$Na_2SiO_3 + 2HNO_3 \rightarrow H_2SiO_3 + 2NaNO_3 \tag{7}$$

$$Na_2SiO_3 + 2HNO_3 \rightarrow SiO_2 + 2NaNO_3 + H_2O \tag{8}$$

$$H_2SiO_3 \rightarrow SiO_2 \bullet nH_2O \tag{9}$$

These reactions contribute to the transformation of silicates, which can have an effect on the structure and properties of the material through the SiO_2 and other products generated.

Mechanisms of porous structure formation

Based on the analysis of elemental composition and micro-morphology, it can be concluded that chemical etching is the key factor in the formation of a porous structure. The strong oxidizing properties of nitric acid lead to the oxidation and etching of the surface of carbon materials, thereby increasing the pore structure. Additionally, nitric acid can generate micropores and mesopores within the residual carbon and silica and silicate by leaching out some of the inorganic components in the gasification slag. The oxidative decomposition of organic matter and the dissolution of inorganic matter not only increase the specific surface area of the material but also create more active adsorption sites within the material.

Under hydrothermal conditions, the gases generated by the nitric acid reaction (e.g., CO_2 and NO_2) generate pressure inside the carbon material, leading to swelling and cracking. While this process generates new pores, it may also cause the collapse of the carbon structure due to excessive force, as described in Section "Impact on the microscopic surface morphology". Therefore, proper control of the nitric acid treatment concentration, duration, and temperature is crucial. The optimal hydrothermal nitric acid treatment conditions are provided in Figure S2.

Nitric acid treatment disrupts the lattice structure of carbon materials, leading to an increase in amorphous carbon and the formation of defect sites, as described in Section "Influence on the microstructure of carbon crystals". These amorphous carbon and defect sites contribute to the formation of a porous structure and provide more active sites for adsorption. Nitric acid treatment also significantly affects the lattice structure of the inorganic components, influencing the adsorption properties of the material during the mineral morphology transformation process. Therefore, the conditions of nitric acid treatment need to be carefully controlled to achieve the optimal preparation of adsorbent materials.

Structure–property correlation mechanism

Nitric acid treatment significantly enhances the adsorption performance of CGFS-X. This treatment markedly increases the specific surface area of the material by generating a porous structure, thereby providing more active sites for the adsorption process. Additionally, nitric acid treatment introduces a substantial number of oxygen-containing functional groups (such as carboxyl, hydroxyl, and nitro groups), which increase the polarity and chemical reactivity of the carbon material, thereby facilitating more efficient adsorption of polar pollutants. Moreover, nitric acid treatment leads to an increase in the amorphous carbon content and the formation of defect sites within the carbon matrix. These defect sites act as active centers, significantly enhancing the adsorption capacity and selectivity of the material. By precisely controlling the concentration of nitric acid and treatment conditions, the pore size distribution of the material can be tailored to better accommodate the adsorption of molecules or ions of specific dimensions. Through the synergistic effects of these mechanisms, hydrothermal nitric acid treatment significantly improves the adsorption performance of CGFS-X for MB removal.

Conclusion

This study employed a one-step hydrothermal nitric acid treatment of CGFS to successfully prepare porous materials with significantly enhanced adsorption performance for MB. Advanced characterization techniques, including N_2 adsorption/desorption experiments, XRD, SEM, FTIR, XPS, and Raman spectroscopy, were utilized to comprehensively analyze the pore structure characteristics, mineral phase composition, surface morphology, surface functional group composition, and carbon microstructure of the samples.

The experimental results revealed that nitric acid treatment not only promoted the development of the pore structure of CGFS, increasing the specific surface area and total pore volume, but also effectively removed partial metal oxides and introduced abundant oxygen-containing functional groups and defect sites on the material's surface. These defect sites, acting as active centers, significantly enhanced the material's adsorption capacity for MB. Notably, the CGFS-2 M sample, obtained by treatment with 2 mol/L nitric acid, exhibited the optimal adsorption performance with an equilibrium adsorption capacity of up to 210.20 mg/g. This result is attributed to the synergistic effect of the optimized porous structure, increased surface active groups, and defects in the carbon crystal microstructure.

The hydrothermal nitric acid treatment method used in this study not only simplifies the preparation process and reduces the preparation cost but also significantly enhances the performance of CGFS-based porous adsorption materials without increasing the environmental burden. By precisely controlling the concentration of nitric acid and treatment conditions, this study provides an effective strategy for the high-value utilization of CGFS.

Based on the previous comparison of the removal effects of CGFS-X (1 M, 2 M, 4 M) on MB and coupled with structural analysis, it can be concluded that multiple strategies should be employed to develop high-performance adsorbent materials. These strategies include enhancing the specific surface area of the materials, optimizing the pore size distribution, and increasing the number of adsorption sites within the materials. For complex solid wastes such as CGFS, it is essential to simultaneously optimize both organic and inorganic components to maximize adsorption performance.

Data availability

The data involved in this study can be found within the main text and the supplementary information files. For any further inquiries or requests regarding the data, please contact Hua Wang at email 99452715@qq.com.

Received: 2 July 2024; Accepted: 3 September 2024
Published online: 11 September 2024

References

1. Lv, B. *et al.* Enrichment and utilization of residual carbon from coal gasification slag: A review. *Process Saf. Environ. Prot.* **171**, 859–873 (2023).
2. Zhang, J. *et al.* Kinetic analysis on the mesoporous formation of coal gasification slag by acid leaching and its thermal stability. *Solid State Sci.* **100**, 106084 (2020).
3. Yan, S., Xuan, W., Cao, C. & Zhang, J. A review of sustainable utilization and prospect of coal gasification slag. *Environ. Res.* **238**, 117186 (2023).
4. Miao, Z., Guo, Z., Qiu, G., Zhang, Y. & Wu, J. Synthesis of activated carbon from high-ash coal gasification fine slag and their application to CO2 capture. *J. CO2 Util.* **50**, 101585 (2021).
5. Peng, D. *et al.* Preparation of a chitosan/coal gasification slag composite membrane and its adsorption and removal of Cr (VI) and RhB in water. *Molecules* **27**, 7173 (2022).
6. Wu, Y.-H. *et al.* Graded synthesis of highly ordered MCM-41 and carbon/zeolite composite from coal gasification fine residue for crystal violet removal. *J. Clean. Prod.* **277**, 123186 (2020).
7. Liu, S., Wei, J., Chen, X., Ai, W. & Wei, C. Low-cost route for preparing carbon-silica composite mesoporous material from coal gasification slag: Synthesis, characterization and application in purifying dye wastewater. *Arab. J. Sci. Eng.* **45**(6), 4647–4657 (2020).
8. Chen, S., Han, B., Chen, X., Xu, F. & Wang, G. Hydrothermal synthesis and morphology control mechanism of $BaTiO_3$ from $NaTi_3O_6(OH)(H_2O)2$ precursors. *Ceram. Int.* **50**(12), 21779–21787 (2024).
9. Aouaini, F. *et al.* Statistical physics analysis of the adsorption of reactive red 141 dye on residual avocado peel (Persea americana) chemically modified with H_2SO_4 and HNO_3. *Inorg. Chem. Commun.* **165**, 112547 (2024).
10. Eskanazy, G., Finkelman, R. B. & Chattarjee, S. Some considerations concerning the use of correlation coefficients and cluster analysis in interpreting coal geochemistry data. *Int. J. Coal Geol.* **83**(4), 491–493 (2010).
11. Saha, S., Madhurina, M. Trace element geochemistry and mineralogy of coal from Samaleswari open cast coal block (S-OCB), Eastern India. *Phys. Chem. Earth* **104**, 47–57 (2018).
12. Shao, S., Ma, B. & Wang, C. Extraction of valuable components from coal gangue through thermal activation and HNO_3 leaching. *J. Ind. Eng. Chem.* **113**, 564–574 (2022).
13. Shi, S., Ma, B., Shao, S., Chen, Y. & Wang, C. Phase diagram of the $Al(NO_3)3$-$Fe(NO_3)3$–H_2O(-HNO_3) system and its application in the separation of Al3+and Fe3+. *J. Chem. Eng. Data* **68**(2), 441–450 (2023).
14. Zhu, D. *et al.* Carbon-silica mesoporous composite in situ prepared from coal gasification fine slag by acid leaching method and its application in nitrate removing. *Sci. Total Environ.* **707**, 136102 (2020).
15. Vassileva, S. V., Menendez, R., Alvarez, D., Diaz-Somoano, M. & Martinez-Tarazona, M. Phase-mineral and chemical composition of coal fly ashes as a basis for their multicomponent utilization. 1. Characterization of feed coals and fly ashes. *Fuel* **82**(14), 1793–1811 (2003).
16. Wu, S., Huang, S., Wu, Y. & Gao, J. Characteristics and catalytic actions of inorganic constituents from entrained-flow coal gasification slag. *J. - Energy Instit.* **88**(1), 93–103 (2015).
17. Wesełucha-Birczyńska, A., Babe, K. & Jurewicz, K. Carbonaceous materials for hydrogen storage investigated by 2D Raman correlation spectroscopy. *Vibrat. Spectrosc.* **60**, 206–211 (2012).
18. Jin, H. *et al.* Graphitized activated carbon based on big bluestem as an electrode for supercapacitors. *RSC Adv.* **4**, 14136 (2014).
19. Wu, S., Huang, S., Ji, L., Wu, Y. & Gao, J. Structure characteristics and gasification activity of residual carbon from entrained-flow coal gasification slag. *Fuel* **122**, 67–75 (2014).
20. Ren, L. *et al.* Effect of oxidation treatment on structural characteristics and combustion behavior of residual carbon from coal gasification fine slag. *Chem. Eng. Sci.* **286**, 119697 (2024).
21. Sadezky, A., Muckenhuber, H., Grothe, H., Niessner, R. & Pöschl, U. Raman microspectroscopy of soot and related carbonaceous materials: Spectral analysis and structural information. *Carbon* **43**(8), 1731–1742 (2005).
22. Jones, S. P., Fain, C. C. & Edie, D. D. Structural development in mesophase pitch based carbon fibers produced from naphthalene. *Carbon* **35**(10), 1533–1543 (1997).
23. Jawhari, T., Roid, A. & Casado, J. Raman spectroscopic characterization of some commercially available carbon black materials. *Carbon* **33**(11), 1561–1565 (1995).
24. Ishimaru, K., Hata, T., Bronsveld, P., Nishizawa, T. & Imamura, Y. Characterization of sp2- and sp3-bonded carbon in wood charcoal. *J. Wood Sci.* **53**(5), 442–448 (2007).
25. Liu, X. *et al.* Coal macromolecular structural characteristic and its influence on coalbed methane adsorption. *Fuel* **222**, 687–694 (2018).
26. Xu, J., Lu, Q., Wu, X. & Liu, D. The fractal characteristics of the pore and development of briquettes with different coal particle sizes. *Chongqing Daxue Xuebao/J. Chongqing Univ.* **34**(9), 81–89 (2011).
27. Wang, Z. *et al.* Experimental study on geometric parameters of pore structure and quantitative evaluation of complexity of pulverized coal with different metamorphic degrees. *Adv. Powder Technol.* **33**, 103764 (2022).
28. Guo, B. *et al.* Experiment and regeneration kinetic model study on CO2 adsorbent prepared from fly ash. *Chem. Eng. J.* **421**(2), 127865 (2021).
29. Deng, G. Z. & Zheng, R. Micropore structure and fractal characteristics of low-permeability coal seams. *Adv. Mater. Sci. Eng.* **2018**, 1–15 (2018).
30. Zhu, Y., Liu, H., Wang, T., Wang, Y. & Liu, H. Evolution of pore structures and fractal characteristics of coal-based activated carbon in steam activation based on nitrogen adsorption method. *Powder Technol.* **424**, 118522 (2023).
31. Wu, Y. H., Ma, Y. L., Sun, Y. G., Xue, K. & Ji, W. X. Graded synthesis of highly ordered MCM-41 and carbon/zeolite composite from coal gasification fine residue for crystal violet removal. *J. Clean. Prod.* **277**, 123186 (2020).
32. Wu, Y. H., Ma, Y. L., Sun, Y. G., Ji, W. X. & Miao, Q. Effects of acid ionization on the formation mechanism of bimodal mesoporous Al-MCM-41s from coal gasification fine residue and evaluation of adsorption capabilities. *J. Hazardous Mater.* **417**(27), 126052 (2021).

33. He, C., Li, Q., Li, P., Wang, Y. & Hao, Z. Templated silica with increased surface area and expanded microporosity: Synthesis, characterization, and catalytic application. *Chem. Eng. J.* **162**(3), 901–909 (2010).
34. Huo, W. *et al.* Mechanical strength of highly porous ceramic foams with thin and lamellate cell wall from particle-stabilized foams. *Ceram. Int.* **44**, 5780–5784 (2017).
35. Zhang, J. B., Li, S. P., Li, H. Q. & He, M. M. Acid activation for pre-desilicated high-alumina fly ash. *Fuel Process. Technol.* **151**(OCT), 64–71 (2016).
36. Silica extractionprocess from rice husk ash. *African Farming and Food Processing* **2016,** (Nov./Dec.).
37. Wang, J. *et al.* Evolution and correlation of the physiochemical properties of bamboo char under successive pyrolysis process. *Biochar* **6**(1), 33 (2024).
38. Isaacs, M. A. *et al.* Advanced XPS characterization: XPS-based multi-technique analyses for comprehensive understanding of functional materials. *Mater. Chem. Front.* **5**(22), 7931–7963 (2021).
39. Khabushev, E. M. *et al.* High-temperature adsorption of nitrogen dioxide for stable, efficient, and scalable doping of carbon nanotubes. *Carbon* **224**, 119082 (2024).
40. Wang, Y. *et al.* Preferential molecular fractionation of dissolved organic matter by iron minerals with different oxidation states. *Chem. Geol.* **520**, 69–76 (2019).
41. Szlachta, M., Gerda, V. & Chubar, N. Adsorption of arsenite and selenite using an inorganic ion exchanger based on Fe–Mn hydrous oxide. *J. Colloid Interface Sci.* **365**(1), 213–221 (2012).
42. Mendoza, A., Guzmán, G., Rivero, I., Camacho-López, S. & Herrera-Zaldivar, M. Point defects and oxygen deficiency in GaN nanoparticles decorating GaN: O nanorods: An XPS and CL study. *Appl. Phys. A* **127**, 1–10 (2021).
43. Cen, Z., Kang, Y., Lu, R. & Yu, A. Electrostatic interaction mechanism of visible light absorption broadening in ion-doped graphitic carbon nitride. *RSC Adv.* **11**(37), 22652–22660 (2021).
44. Li, X. *et al.* One step synthesis of Mo-doped carbon microspheres for valorization corncob to levulinic acid. *Ind. Crops Prod.* **184**, 115019 (2022).
45. Chubar, N., Gerda, V., Szlachta, M. & Yablokova, G. Effect of Fe oxidation state (+ 2 versus+ 3) in precursor on the structure of Fe oxides/carbonates-based composites examined by XPS FTIR and EXAFS. *Solid State Sci.* **121**, 106752 (2021).
46. Tang, C. & Dong, H. The effects of Cu2+ adsorption on surface dissolution of albite. *Colloids Surfaces A Physicochem. Eng. Aspects* **644**, 128832 (2022).
47. Cheng, M. *et al.* High adsorption of methylene blue by salicylic acid-methanol modified steel converter slag and evaluation of its mechanism. *J. Colloid Interface Sci.* **515**, 232–239 (2018).
48. Bhuyan, M. A. H. & Luukkonen, T. Adsorption of methylene blue by composite foams containing alkali-activated blast furnace slag and lignin. *Int. J. Environ. Sci. Technol.* **21**(4), 3789–3802 (2024).
49. Bhuyan, M. A. H., Gebre, R. K., Finnila, M. A. J., Illikainen, M. & Luukkonen, T. Preparation of filter by alkali activation of blast furnace slag and its application for dye removal. *J. Environ. Chem. Eng.* **10**(1), 107051 (2022).
50. Dinh, N. T., Vo, L. N. H., Tran, N. T. T., Phan, T. D. & Nguyen, D. B. Enhancing the removal efficiency of methylene blue in water by fly ash via a modified adsorbent with alkaline thermal hydrolysis treatment. *RSC Adv* **11**(33), 20292–20302 (2021).
51. Zhang, Y. *et al.* Synthesis of porous material from coal gasification fine slag residual carbon and its application in removal of methylene blue. *Molecules* **26**(20), 6116 (2021).
52. Liu, S., Chen, X., Ai, W. & Wei, C. A new method to prepare mesoporous silica from coal gasification fine slag and its application in methylene blue adsorption. *J. Clean. Prod.* **212**, 1062–1071 (2019).
53. Zhou, J. *et al.* Tuning the reactivity of carbon surfaces with oxygen-containing functional groups. *Nat. Commun.* **14**(1), 2293 (2023).
54. Matinfar, M. & Nychka, J. A. A review of sodium silicate solutions: Structure, gelation, and syneresis. *Adv. Colloid Interface Sci.* **322**, 103036 (2023).

Acknowledgements

The authors would like to extend their heartfelt gratitude to the following funding sources for their generous financial support in facilitating this research project:National Natural Science Foundation of China (Grant No. 22168043), Key Scientific Research Program of the Shaanxi Provincial Department of Education (Project No. 23JS064), Graduate Student Innovation Fund Project (Project No. 2023YLYCX12), Joint Project between Yulin University and the Chinese Academy of Sciences (Project No. YLUDNL202201), and Youth innovation team project of Shaanxi Province Education Department (Grant No. 23JP204). The invaluable support provided by these organizations has made a significant contribution to the successful completion of this study.

Author contributions

Hua Wang contributed to the experimental design and performed the hydrothermal treatment experiments. Yunxuan Luoyang was responsible for the synthesis of the porous materials and the characterization of their adsorption properties. Jian Li conducted the analysis of the adsorption kinetics and isotherms. Xia Li prepared the graphical abstract and Figs. 1–3, illustrating the experimental procedures and results. Bi Chen contributed to the interpretation of data and the writing of the initial draft. Guotao Zhang supervised the project, provided critical feedback, and finalized the manuscript. All authors discussed the results, contributed to the final version of the manuscript, and agreed on the submission to Scientific Reports.

Competing interests

The authors declare no competing interests.

Additional information

Supplementary Information The online version contains supplementary material available at https://doi.org/10.1038/s41598-024-72114-7.

Correspondence and requests for materials should be addressed to H.W.